Monthly Notices of the ROYAL ASTRONOMICAL SOCIETY
MNRAS **504,** 3651–3661 (2021)
Advance Access publication 2021 March 19
doi:10.1093/mnras/stab809

# Application of a new X-ray reflection model to V1223 Sagittarii

Takayuki Hayashi,[1,2]★ Takao Kitaguchi[3,4] and Manabu Ishida[5,6]

[1] *NASA, Goddard Space Flight Center, Code 662, Greenbelt, MD 20771, USA*
[2] *Department of Physics, University of Maryland, Baltimore County, 1000 Hilltop Circle, Baltimore, MD 21250, USA*
[3] *RIKEN Cluster for Pioneering Research, 2-1 Hirosawa, Wako, Saitama 351-0198, Japan*
[4] *RIKEN Nishina Center, 2-1 Hirosawa, Wako, Saitama 351-0198, Japan*
[5] *The Institute of Space and Astronautical Science/JAXA, 3-1-1 Yoshinodai, Chuo-ku, Sagamihara 252-5210, Japan*
[6] *Department of Physics, Tokyo Metropolitan University, 1-1 Minami-Osawa, Hachioji, Tokyo 192-0397, Japan*

Accepted 2021 March 12. Received 2021 March 10; in original form 2020 October 19



## ABSTRACT

In intermediate polars (IPs), the intrinsic thermal emissions from white dwarfs (WDs) have typically been studied. Few reports have analysed X-ray reflections from WDs. We recently developed an elaborate IP-reflection spectral model. Herein, we report the first application of a reflection model with an IP thermal model to the spectra of the brightest typical IP V1223 Sagittarii observed by the *Suzaku* and *Nuclear Spectroscopic Telescope Array* satellites. The model reasonably reproduces the spectra within the range of 5–78 keV and estimates the WD mass as $0.92 \pm 0.02\,M_\odot$. The WD mass estimated by the proposed model is consistent with that measured using an active galactic nucleus reflection model and a partial covering absorption model. However, the choice of incorrect parameter values, such as an unsuitable fitting energy band and an incorrect metal abundance, was found to introduce systematic errors (e.g. $\lesssim 0.2\,M_\odot$ in the WD mass) in the WD mass measurement. Our spin-phase-resolved analysis resulted in discoveries regarding the modulations of the equivalent width of the fluorescent iron K $\alpha$ line and the angle between the post-shock accretion column and the line of sight (viewing angle). The viewing angle anticorrelates approximately with the X-ray flux and has average and semi-amplitude values of 55° and 7°, respectively, which points towards two WD spin axis angles from the line of sight of 55° and 7°, respectively. Both estimated spin axis angles are different from the reported system inclination of 24°.

**Key words:** accretion, accretion discs – methods: data analysis – fundamental parameters – cataclysmic variables – white dwarfs – X-rays: binaries.

## 1 INTRODUCTION

Cataclysmic variables (CVs) are close binary systems consisting of a companion late-type main-sequence star and a white dwarf (WD). The late-type star fills the Roche lobe and feeds its gaseous material to the WD through the inner Lagrange point. CVs comprising a highly magnetized WD ($B > 0.1$ MG) are called magnetic CVs (mCVs), which are categorized as polar or intermediate polar (IP) systems. In polar systems, the magnetic field is quite strong ($B > 10$ MG) and can channel the gaseous flow directly from the companion star. In IPs, the magnetic field is moderate ($0.1 < B < 10$ MG), and an accretion disc forms around the WD. The magnetic field tears the gas from the accretion disc near the Alfvén radius and channels it. The channelled gas falls towards the WD at an almost free-fall velocity and is accelerated up to hypersonic speeds. A strong shock is formed close to the WD surface, heats the gas, and generates highly ionized plasma. In IP systems, the plasma flow is cooled by an X-ray thermal emission, and the plasma flow then settles on to the WD surface, which is called the post-shock accretion column (PSAC). The PSAC irradiates the WD with X-rays, and the WD shines in the X-ray owing to the reflection.

The X-ray observation enables us to measure the WD mass independent of the dynamical measurement and to determine the PSAC geometry. The WD model is still controversial, particularly under extreme conditions (e.g. Yoon & Langer 2004; Das, Mukhopadhyay & Rao 2013), and the WD mass is a fundamental physical parameter used to constrain the model. However, the well-established dynamic WD mass measurement is difficult, except in systems showing an eclipse because of the uncertainty in the orbital inclination angle. By contrast, with X-ray spectroscopy, the WD mass can be measured by measuring the plasma temperature, which is correlated with the gravitational potential. Moreover, the reflection enables us to measure the height of the PSAC and the angle between the PSAC and the line of sight. Height is a fundamental parameter that specifies the PSAC and constrains the WD mass. The PSAC angle is modulated by the WD spin, which allows us to estimate the spin axis angle. The spin axis angle provides the direction of the angular momentum, which is new information regarding the dynamics of a binary system.

The thermal X-ray spectrum of PSAC has been well studied. The PSAC has been hydrodynamically modelled (Aizu 1973; Hōshi 1973; Imamura & Durisen 1983; Wu, Chanmugam & Shaviv 1994; Woelk & Beuermann 1996; Cropper, Ramsay & Wu 1998; Cropper et al. 1999; Canalle et al. 2005; Saxton et al. 2005, 2007; Hayashi & Ishida 2014a). Such studies involved various physical effects:

★ E-mail: thayashi@umbc.edu

**Table 1.** Observation summary of V1223 Sgr by *Suzaku* and *NuSTAR*.

| Observation ID | Observation date (UT) | Data set name | Aim point | Detector | Exposure (ks)$^{a}$ |
|---|---|---|---|---|---|
| | | *Suzaku* | | | |
| 402002010 | 2007 April 13–14th | 07S | HXD | XIS | 60.7 |
| | | | | HXD | 46.3 |
| 408019010 | 2014 March 29–30th | 14S | XIS | XIS | 29.4 |
| | | | | HXD | 26.1 |
| 408019020 | 2014 April 10–14th | – | XIS | XIS | 150.8 |
| | | | | HXD | 146.3 |
| | | *NuSTAR* | | | |
| 30001144002 | 2014 September 16 | 14N | – | FPMA/FPMB | 20.4 |

[a]Exposure time after data screening.

gravitational potential release, cross-section convergence, and variation in the accretion rate per unit area (called the 'specific accretion rate'). PSAC models have been employed to measure the WD mass of the mCVs (Ishida et al. 1991; Fujimoto & Ishida 1997; Cropper et al. 1998, 1999; Ezuka & Ishida 1999; Ramsay et al. 2000; Suleimanov, Revnivtsev & Ritter 2005; Brunschweiger et al. 2009; Landi, Bassani & Dean 2009; Yuasa et al. 2010; Hayashi & Ishida 2014b).

Less attention has been paid to the X-ray reflection from the WD surface despite its prominent spectral features. The reflection consists of thermal X-rays escaping from the WD through scattering and/or fluorescence. The reflection spectrum has distinctive features: fluorescent iron K $\alpha$ lines, a Compton hump at approximately 10–30 keV, and Compton shoulders following the emission lines. These features enable us to study the geometry between a PSAC and a WD. However, these features can be a nuisance when obtaining thermal plasma parameters unless they are correctly modelled.

Several studies have considered the reflection in their spectral analysis (e.g. Beardmore et al. 1995; Cropper et al. 1998; Beardmore, Osborne & Hellier 2000; Hayashi et al. 2011; Mukai et al. 2015; Shaw, Heinke & Mukai 2018), invoking reflection models developed for active galactic nuclei (AGNs; e.g. George & Fabian 1991; Magdziarz & Zdziarski 1995) or for the mCV (van Teeseling, Kaastra & Heise 1996). However, these models do not incorporate the stratified structure of the PSAC, finite height of the PSAC, or the WD curvature. Moreover, the features incurred by the scattering and fluorescence were handled separately.

Recently, we developed an IP reflection model using a Monte Carlo simulation (Hayashi, Kitaguchi & Ishida 2018). In the model, a finite-length columnar source on a spherical reflector irradiated the reflector with X-rays, the spectrum of which was determined by the PSAC stratified structure calculated by Hayashi & Ishida (2014a). The reflector was cold and neutral, and its radius was determined based on the WD mass (Nauenberg 1972). The simulation involved X-ray interactions with atoms, i.e. coherent/incoherent scattering and photoelectric absorption. The photoelectric absorption by iron and nickel is followed by K $\alpha_{1,2}$ and K $\beta$ fluorescent emissions with the corresponding fluorescent yield. The reflection model has five fitting parameters: the WD mass ($M_{\rm WD}$), specific accretion rate ($a$), elemental abundance ($Z$), the angle between the PSAC and line of sight ($i$), and normalization. These parameters are common to the IP thermal model of Hayashi & Ishida (2014a).

We selected V1223 Sagittarii (V1223 Sgr) as the first target to demonstrate how well the IP reflection model reproduces the observed spectrum and the parameters that can be measured. V1223 Sgr is a typical IP and one of the brightest. The other brightest IPs, EX Hydrae and V2400 Ophiuchus, are somewhat extraordinary owing to their extremely low X-ray luminosity (Suleimanov et al. 2005) and the discless feature (Buckley et al. 1995), respectively. V1223 Sgr was observed for 240 and 20 ks using the *Suzaku* and *Nuclear Spectroscopic Telescope Array* (*NuSTAR*) satellites, respectively (Section 2), the data of which are publicly available. The *Suzaku* data have a large effective area for fluorescent iron K $\alpha$ lines, and the fluorescent line was resolved from the thermal K $\alpha$ lines. The *NuSTAR* data have a high signal-to-noise ratio in the Compton hump energy band.

In this paper, we present an application of the IP reflection model to the V1223 Sgr data acquired by the *Suzaku* and *NuSTAR* satellites. We describe the observations and data reduction in Section 2 and the model application in Section 3. We discuss the reflection spectral modelling, the effects of various parameters on the WD mass estimation, and the geometry in Section 4. The conclusions are presented in Section 5.

## 2 OBSERVATIONS AND DATA REDUCTION

We used *Suzaku* (Mitsuda et al. 2007) and *NuSTAR* (Harrison et al. 2013) archival data for V1223 Sgr. Table 1 shows a summary of the observation. We applied a barycentric correction to each data set (Terada et al. 2008).

### 2.1 *Suzaku*

*Suzaku* has two instruments: an X-ray imaging spectrometer (XIS; Koyama et al. 2007) and a hard X-ray detector (HXD; Kokubun et al. 2007; Takahashi et al. 2007). The XIS has an imaging capability with the aid of an X-ray Telescope (XRT; Serlemitsos et al. 2007). The 2007 and 2014 observations (hereafter referred to as 07S and 14S, respectively) were conducted at the nominal positions of the HXD and XIS, respectively. The exposure time is tabulated in Table 1. The 07S and 14S data were screened through the *Suzaku* processing pipeline version 3.0.22.43 and 3.0.22.44, respectively, with the latest calibration data base (20160607 for XIS, 20110630 for XRT, and 20110913 for HXD).

#### *2.1.1 XIS*

We extracted the source events from a circle of radius 4.′34 around the image centre. The background events fall in the annulus between radii of 4.′34 and 8.′68, excluding those regions irradiated by the $^{55}$Fe calibration sources and the detector edges. One of the XIS sensors XIS0 in 14S has an unusable area owing to an anomaly that was also excluded from the background region. The spectra of the two front-illuminated (FI) sensors (XIS0 and 3) were combined. During all of the observations, the other FI sensor XIS2 was deemed unusable because of an anomaly that occurred in 2006 November. Subsequently, the data acquired during the two periods in 2014 were combined.

#### 2.1.2 *HXD-PIN*

We used the 'tuned' non-X-ray background (NXB) spectrum version 2.0 provided by the instrument team (Fukazawa et al. 2009) for the 07S HXD-PIN data. The cosmic X-ray background (CXB) spectrum was generated by convolving the spectral model of Boldt (1987) with the detector response. The NXB and CXB spectra were subtracted from the HXD-PIN data. We did not use the S14 HXD-PIN data because only a 'quick' NXB spectrum was provided, which had larger systematic errors.

### 2.2 *NuSTAR*

*NuSTAR* has two co-aligned hard XRTs. Each telescope focuses celestial X-rays on to a focal plane module A or B (FPMA or FPMB). The observation of V1223 Sgr was conducted in 2014 September (hereafter referred to as 14N). We reprocessed the data using the *NuSTAR* data analysis software (`NuSTARDUS` v.1.7.1) and the calibration files of 20171002 to extract the cleaned events. The source events were extracted within a circle of 2.′5 radii around the image centre, whereas the background events were extracted within an annulus between radii of 2.′5 and 5.′0 by excluding the detector edges.

## 3 SPECTRAL MODEL FITTING

The IP thermal model of Hayashi & Ishida (2014a) and the reflection model of Hayashi et al. (2018) (hereafter referred to as ACRAD$_{\rm TH}$ and ACRAD$_{\rm REF}$, respectively) have been compiled into table models that are available on the XSPEC (Arnaud 1996). We fitted the IP models to the V1223 Sgr spectrum using XSPEC version 12.9.1, binding the same parameters in both models. For comparison, we also fitted an AGN reflection model (REFLECT in XSPEC; Magdziarz & Zdziarski 1995) or a partial covering absorption (PCA) model (PCFABS in XSPEC) instead of ACRAD$_{\rm REF}$. Phenomenologically, the PCA model may reproduce the spectral shape of the Compton hump (Cropper et al. 1998). With REFLECT and PCFABS, a narrow Gaussian model was added to the fluorescent iron K$\alpha$ line, whose central energy and width were fixed at 6.4 and 0 keV, respectively. The abundances of iron and other elements in REFLECT were bound to that of ACRAD$_{\rm TH}$. For all cases, the photoelectric absorption was considered using PHABS. In summary, we used the three models of PHABS × (ACRAD$_{\rm TH}$ + ACRAD$_{\rm REF}$), PHABS × (REFLECTING × ACRAD$_{\rm TH}$ + GAUSSIAN), and PHABS × (PCFABS × ACRAD$_{\rm TH}$ + GAUSSIAN), which are hereafter referred to as `IP-reflect`, `AGN-reflect`, and `PCA-reflect`, respectively. We excluded data below 5 keV to avoid the complicated absorption feature created by the multicolumnar absorber (Ezuka & Ishida 1999). The exclusion of <5 keV data is reasonable because the main features of the maximum plasma temperature depending on the WD mass and the reflection appear at above 5 keV.

### 3.1 Spin-averaged spectrum

First, we fitted each model to the spin-averaged spectra of all data sets. Figs 1, 2, and 3 display the spectrum with the best-fitting models, and Table 2 shows the best-fitting parameters. The three fittings are comparable in terms of the goodness of fit. In other words, the `PCA-reflect` model reproduces the Compton hump as much as the `IP-reflect` and `AGN-reflect` models do, although the parameters of PCFABS in `PCA-reflect` have no physical meaning. Here, `IP-reflect` estimated the WD mass $M_{\rm WD}$ to be 0.86 ± 0.01 M$_{\odot}$, which is consistent with $M_{\rm WD}$ = 0.87 ± 0.01 and 0.83 ± 0.02 M$_{\odot}$

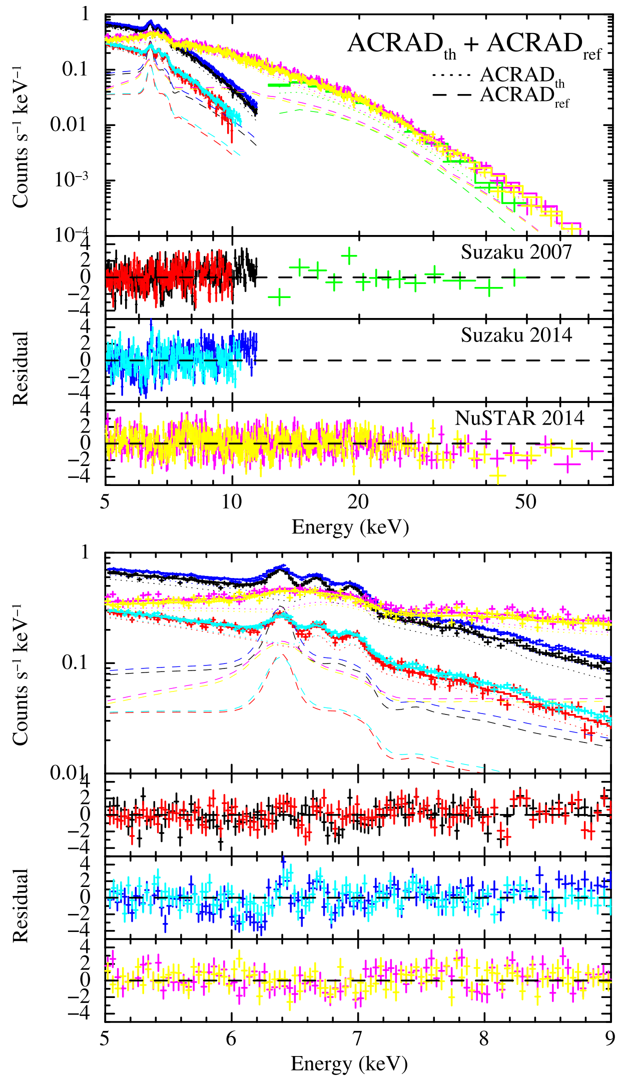


**Figure 1.** Top: 07S-FI (black), 07S-BI (red), 07S-PIN (green), 14S-FI (blue), 14S-BI (light blue), 14N-FPMA (magenta), and 14N-FPMB (yellow) spectra with the best-fitting `IP-reflect` model. The three lower panels show the residuals of 07S, 14S, and 14N from the top in units of $\sigma$. The dotted and dashed lines show the thermal (ACRAD$_{\rm TH}$) and reflection (ACRAD$_{\rm REF}$) components, respectively. Bottom: Blowup of top panel between 5 and 9 keV.

estimated by `AGN-reflect` and `PCA-reflect`, respectively. All three models estimated an extremely high specific accretion rate, with log ($a$ [g cm$^{-2}$ s$^{-1}$]) > 2, and were found to agree with each other. In addition, `IP-reflect` tightly constrained the viewing angle to $i = 54.2^{-2.2}_{+2.1}$ °, which disagrees with the output of `AGN-reflect` of $i$ < 42 °. The shock height $h$ and the maximum plasma temperature $T_{\rm max}$ (i.e. the temperature just below the shock) are hydrodynamically calculated (Hayashi & Ishida 2014a) using the best-fitting parameters, as shown in Table 2. The luminosity of the thermal component within the 0.1–100 keV band is estimated as $1 \times 10^{34}$ erg s$^{-1}$ by all three models with the distance $D = 580 \pm 16$ pc set as per *Gaia* Data Release 2 (Gaia Collaboration 2016).

The change in accretion rate affects the specific accretion rate and hydrogen column density. With this in mind, we fitted `IP-reflect` again, separating the specific accretion rate and the hydrogen column density into different data sets. Table 3 shows the best-fitting parameters. The fitting was found to improve statistically,

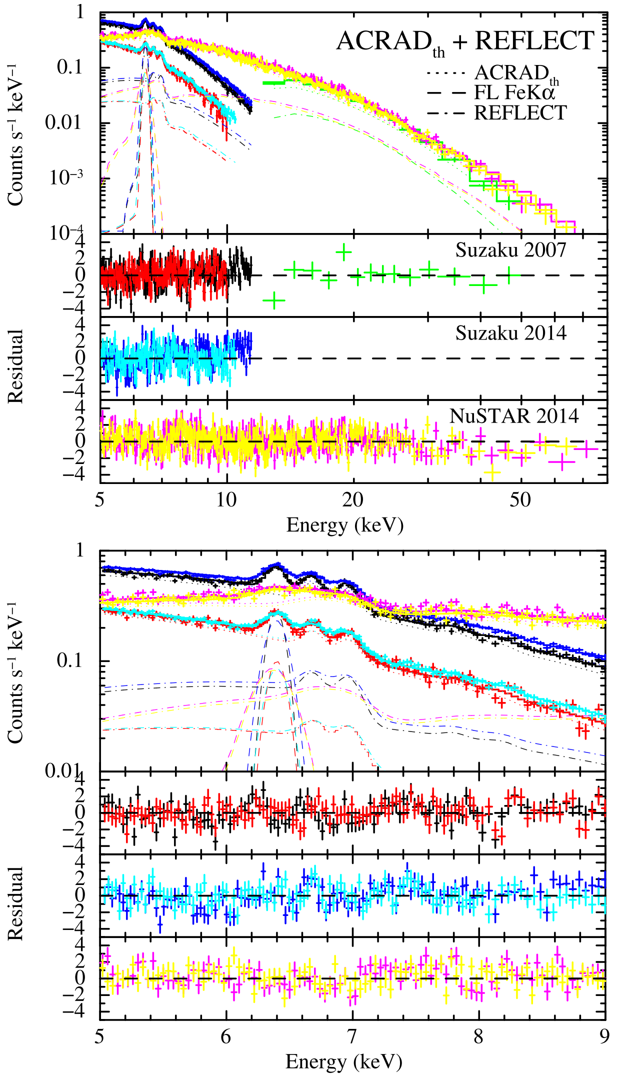


Figure 2. Same as Fig. 1, although the fitting model is `AGN-reflect`. The dotted, dotted–dashed, and dashed lines show the thermal (ACRAD$_{TH}$), fluorescent iron K $\alpha$ line (GAUSSIAN), and reflection (REFLECT) components, respectively.

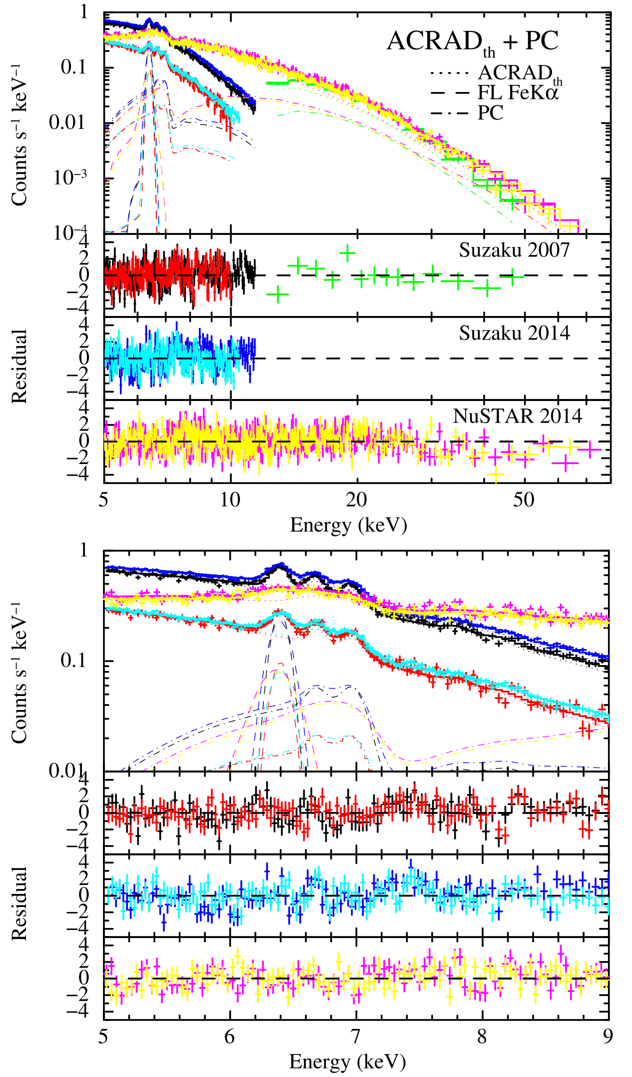


Figure 3. Same as Fig. 1, although the fitting model is `PCA-reflect`. Dotted, dotted–dashed, and dashed lines show the thermal (ACRAD$_{TH}$), fluorescent iron K $\alpha$ line (GAUSSIAN), and reflection (PCFABS) components, respectively.

with the *F*-test indicating that the significance in separating the parameters is 1–2 $\times$ $10^{-9}$. The specific accretion rate and the hydrogen column density are consistent between 07S and 14S. By contrast, both parameters of 14N are less than those of the other data sets, which is qualitatively self-consistent. The WD mass $M_{\rm WD}$ = 0.92 $\pm$ 0.02 $M_\odot$ is 0.06 $M_\odot$ higher in mass than that estimated by fitting when binding the specific accretion rate and the hydrogen column density across the entire data set.

### 3.2 Spin-phase-resolved spectrum

We divided the spectrum based on the spin phase with a period of 745.63 s (Osborne et al. 1985). We determined the temporal origin of each data set by cross-correlating the light curves because there was no ephemeris to share among the data sets. We used the 5–10 keV energy band to establish cross-correlations among the *Suzaku* and *NuSTAR* data. As a result, we determined the origins of BJD = 2454203.48031, 2456745.50051, 2456757.50299, and 2456916.50652 for the data of 07S, 14S-March, 14S-April, and 14N, respectively. Panel (a) of Fig. 5 shows the folded light curves. We divided the spectrum into the following eight phases: 0–0.25, 0.125–0.375, 0.25–0.5, 0.375–0.625, 0.5–0.75, 0.625–0.875, 0.75–1.0, and 0.875–1.125. Note that these phases show a mutual overlap of 0.125.

First, we fitted the PHABS $\times$ (POWERLAW + 3 $\times$ GAUSSIANs) model to the spin-phase-resolved spectra. The three GAUSSIANs reproduced the fluorescent, He-like, and H-like iron K $\alpha$ lines at 6.40, 6.70, and 6.97 keV in the rest frames, respectively. We kept the GAUSSIANs narrow and used 5–23 keV to reasonably reproduce the continuum using the power law. Fig. 4 shows the 0–0.25 spin phase spectrum with the best-fitting model. This empirical model appropriately approximates the spectra. The best-fitting energy centroid and the equivalent width (EW) are listed in Table 4 along with $\chi^2$. Panels (c) and (d) of Fig. 5 show the energy centroid and the EW, respectively, as functions of the phase. Both parameters modulate with the WD spin.

Next, we fitted `IP-reflect` to the spin-phase-resolved spectra. We fixed the WD mass, abundance, and specific accretion at their best-fitting quantities of the phase-averaged fitting with the separated specific accretion rate (Table 2). This is because the WD mass and

**Table 2.** Best-fitting parameters of the spectral fitting to the spin-averaged V1223 Sgr spectra for all the data sets*. $T_{max}$ and $h$ were hydrodynamically calculated with the best-fitting parameters (Hayashi & Ishida 2014a).

| Nickname | PHABS × (ACRAD$_{TH}$ + ACRAD$_{REF}$) `IP-reflect` | PHABS × (REFLECT × ACRAD$_{TH}$ + GAUSSIAN) `AGN-reflect` | PHABS × (PCFABS × ACRAD$_{TH}$ + GAUSSIAN) `PCA-reflect` |
|---|---|---|---|
| $N_H$ (× $10^{22}$ cm$^{-2}$) | $6.5 \pm 0.5$ | $8.9 \pm 0.7$ | $8.2^{+2.2}_{-2.5}$ |
| $M_{WD}$ ($M_\odot$) | $0.86 \pm 0.01$ | $0.87 \pm 0.02$ | $0.83 \pm 0.02$ |
| log($a$) (g cm$^{-2}$ s$^{-1}$) | >2.5 | >2.7 | >2.0 |
| $Z$ ($Z_\odot$)[a] | $0.32 \pm 0.01$ | $0.29 \pm 0.01$ | $0.26^{+0.02}_{-0.01}$ |
| $i$ (°) | $54.2^{+2.1}_{-2.2}$ | <42 | – |
| $\Omega/2\pi$ | – | $0.44^{+0.10}_{-0.06}$ | – |
| $N_{H,PCA}$ (× $10^{22}$ cm$^{-2}$)[b] | – | – | $90^{+30}_{-29}$ |
| $CF_{PCA}$[c] | – | – | $0.30^{+0.12}_{-0.05}$ |
| $EW_{Fe\,I-K\alpha}$ (eV)[d] | – | $105^{+15}_{-2}$ | $104 \pm 4$ |
| $F_{bol}$ (× $10^{-10}$ erg s$^{-1}$)[e] | 2.8 | 3.2 | 3.3 |
| $L_{bol}$ (× $10^{34}$ erg s)[f] | 1.1 | 1.3 | 1.3 |
| $f$[g] | $<4 \times 10^{-5}$ | $<3 \times 10^{-5}$ | $<1 \times 10^{-4}$ |
| $\chi^2_{red}$ (d.o.f.) | 1.38 (1196) | 1.31 (1194) | 1.34 (1194) |
| $T_{max}$ (keV)[h] | 42 | 43 | 39 |
| $h$ ($R_{WD}$)[i] | $<4 \times 10^{-4}$ | $<3 \times 10^{-4}$ | $<1 \times 10^{-4}$ |

*The errors indicate a 90 per cent statistical uncertainty.
[a]Based on Anders & Grevesse (1989).
[b]The hydrogen column density of PCA.
[c]The covering fraction of PCA.
[d]The equivalent width of the fluorescent iron K α line.
[e]Unabsorbed flux in 0.1–100 keV without the reflect component.
[f]Unabsorbed luminosity in 0.1–100 keV without the reflect component.
[g]The fractional accreting area.
[h]The temperature just below the shock.
[i]Height of the shock column from the WD surface.

**Table 3.** Best-fitting parameters of the spectral fitting to the spin-averaged V1223 Sgr spectrum with `IP-reflect`*. $a$, $N_H$, and normalization separated into different data sets. The parameters below the dashed line were hydrodynamically calculated using the best-fitting parameters (Hayashi & Ishida 2014a). The superscript signs are the same as those in Table 2.

| Data set | 07S | 14S | 14N |
|---|---|---|---|
| $N_H$(× $10^{22}$ cm$^{-2}$) | $6.3^{+0.8}_{-0.9}$ | $6.5 \pm 0.5$ | $5.5^{+1.2}_{-1.1}$ |
| $M_{WD}$ ($M_\odot$) | | $0.92 \pm 0.02$ | |
| log($a$) (g cm$^{-2}$ s$^{-1}$) | >1.7 | >2.3 | $0.5^{+0.3}_{-0.2}$ |
| $Z$ ($Z^a_\odot$) | | $0.34 \pm 0.01$ | |
| $i$ (°) | | $53.2 \pm 2.1$ | |
| $F^e_{bol}$ (× $10^{-10}$ erg s$^{-1}$) | 2.9 | 2.8 | 2.8 |
| $L^f_{bol}$ (× $10^{34}$ erg s) | 1.2 | 1.1 | 1.1 |
| $f^g$ | $<2 \times 10^{-4}$ | $<6 \times 10^{-5}$ | $4 \times 10^{-3}$ |
| $\chi^2_{red}$ (d.o.f.) | | 1.33 (1192) | |
| $T^h_{max}$ (keV) | 48 | 48 | 46 |
| $h^i$ ($R_{WD}$) | $<4 \times 10^{-3}$ | $<9 \times 10^{-4}$ | $5^{+4}_{-2} \times 10^{-2}$ |

abundance should be independent of the spin phase and the specific accretion is too insensitive to detect its spin modulation. Moreover, we fixed the ratio of the hydrogen column densities of 14S and 14N to that of 07S at 1.03 and 0.88, respectively, which are the best-fitting hydrogen column densities of the phase-averaged fitting. The consistent modulation profiles within the 5–10 keV band across all data sets (panel a of Fig. 5) justify fixing the hydrogen column density ratio. Table 4 shows the best-fitting parameters. Panels (e) and (f) of Fig. 5 display the hydrogen column density of 07S and the viewing angle, respectively, during the spin period. Both parameters modulate with the WD spin as well.

## 4 DISCUSSION

### 4.1 Reflection component

We found a remarkable discrepancy in the reflection parameters (i.e. viewing and solid angles) among the spin-phase-averaged spectral fittings with the bound hydrogen column density and the specific accretion rate (see Table 2). The best-fitting viewing angles of `IP-reflect` and `AGN-reflect` are $i = 54.2^{+2.1}_{-2.2}$° and < 42°, respectively. The best-fitting solid angle of the `AGN-reflect` model was $\Omega/2\pi = 0.44^{+0.10}_{-0.06}$. Assuming a point source, as in REFLECT in

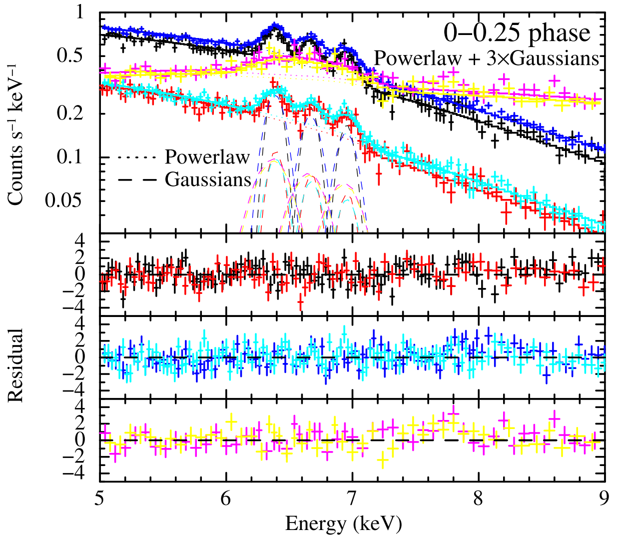


**Figure 4.** The 5–9 keV spectra from the 0–0.25 spin phase with the best-fitting PHABS × (POWERLAW + 3 × GAUSSIANS) model to the 5–23 keV spectra. The relations between the data and colours are the same as in Fig. 1. The dotted and dashed lines show the POWERLAW and three GAUSSIANS, respectively.

AGN-reflect, the solid angle is expressed as

$$\Omega/2\pi = 1 - \sqrt{1 - \frac{1}{\left(\frac{h}{R_{\rm WD}} + 1\right)^2}}. \quad (1)$$

Thus, the PSAC height is calculated at 13 per cent of the WD radius. Note that the PSAC should even be taller with its actual finite length. However, the PSAC is shorter than 0.03 per cent of the WD radius according to the hydrodynamical calculation (Hayashi & Ishida 2014a) with the best-fitting parameters of AGN-reflect, indicating that AGN-reflect is seriously self-inconsistent.

As a major advantage of $\mathrm{ACRAD_{REF}}$ in IP-reflect over other reflection models, it utilizes the fluorescent iron K $\alpha$ line to determine the reflection spectrum. To do so, the other models use a Compton hump, which is a continuum, making it difficult to separate from the thermal continuum. In fact, the solid angle or the viewing angle is generally fixed when using REFLECT (for example, Hayashi et al. 2011; Mukai et al. 2015). By contrast, we tightly constrained both parameters simultaneously using IP-reflect.

To compare the reflection models, the ratios of the best-fitting reflection spectra of AGN-reflect and PCA-reflect to that of IP-reflect are plotted in Fig. 6. In the case of PCA-reflect, the reflection spectrum is the sum of the narrow Gaussian and the thermal spectrum strongly attenuated using the PCA model to mimic the Compton hump. The reflection spectrum of AGN-reflect includes a narrow Gaussian. The ratios have numerous lines that originate from the thermal emission. IP-reflect considers the energy loss to be due to incoherent scattering (Hayashi et al. 2018). PCA-reflect cannot reproduce the energy loss. In addition, REFLECT in AGN-reflect does not calculate the energy loss at below 10 keV (Magdziarz & Zdziarski 1995). Therefore, the thermal-origin emission lines in the reflection spectrum of PCA-reflect and AGN-reflect stay at their original energy, and the total spectrum overestimates the intensity of the thermal emission lines. As a result, the reflection spectrum is inevitably suppressed to match the overestimated model lines to the data. Although either an increase of the viewing angle or a decrease of the solid angle suppresses the reflection, only the latter results in a strong curvature at approximately 20–30 keV (George & Fabian 1991; Hayashi et al. 2018). This stronger curvature reproduces the Compton hump better with the suppressed reflection. As a result, the solid angle is decreased to suppress the reflection. In fact, Mukai et al. (2015) reported that the reflection spectrum reproduced by REFLECT is suppressed when the iron K $\alpha$ lines are included in the fitting. Meanwhile, the overestimated lines also suppressed the abundance, as shown in Table 3. It should be noted that a better energy resolution would strengthen the suppression of the reflection and abundance because it highlights the discrepancy in the overestimated line.

Another noticeable feature in the spectral ratios is the Compton shoulder below the emission lines. Neither PCA-reflect nor AGN-reflect reproduces the Compton shoulder, as described above. More-

**Table 4.** Best-fitting parameters of the spin-phase-resolved spectra with PHABS × (POWERLAW + 3GAUSSIANS) and IP-reflect*.

| Phase | 0.875–1.125 | 0–0.25 | 0.125–0.375 | 0.25–0.5 | 0.375–0.625 | 0.5–0.75 | 0.625–0.875 | 0.75–1 |
|---|---|---|---|---|---|---|---|---|
| | | | | PHABS × (POWERLAW + 3 × GAUSSIANS) | | | | |
| Fe I–K $\alpha$ line energy (keV) | $6.391 \pm 0.005$ | $6.388^{+0.006}_{-0.004}$ | $6.387^{+0.007}_{-0.005}$ | $6.386 \pm 0.007$ | $6.391^{+0.007}_{-0.005}$ | $6.398^{+0.007}_{-0.008}$ | $6.398^{+0.001}_{-0.004}$ | $6.399^{+0.001}_{-0.006}$ |
| Fe I-K $\alpha$ line EW (eV) | $109.7^{+4.1}_{-4.4}$ | $120.8^{+7.4}_{-7.8}$ | $130.1^{+7.2}_{-6.0}$ | $125.9^{+6.9}_{-5.4}$ | $113.1^{+5.1}_{-7.2}$ | $109.7^{+8.2}_{-6.6}$ | $102.5^{+6.3}_{-5.9}$ | $103.6^{+8.8}_{-7.7}$ |
| $\chi^2$ (d.o.f.) | 1.17 (765) | 1.08 (762) | 1.13 (753) | 1.18 (741) | 1.15 (748) | 1.12 (752) | 1.05 (759) | 1.14 (760) |
| | | | | PHABS × ($\mathrm{ACRAD_{TH}}$ + $\mathrm{ACRAD_{REF}}$) | | | | |
| $N_{\rm H,\,07S}$ ($\times\,10^{22}$ cm$^{-2}$) | $4.3^{+0.2}_{-0.3}$ | $6.5^{+0.2}_{-0.3}$ | $9.6 \pm 0.3$ | $11.0 \pm 0.3$ | $8.6 \pm 0.3$ | $5.2^{+0.2}_{-0.3}$ | $3.8^{+0.2}_{-0.3}$ | $3.8^{+0.2}_{-0.3}$ |
| $N_{\rm H,14S}$ ($\times\,10^{22}$ cm$^{-2}$)$^a$ | 4.4 | 6.6 | 9.9 | 11.3 | 8.9 | 5.3 | 3.9 | 3.9 |
| $N_{\rm H,14N}$ ($\times\,10^{22}$ cm$^{-2}$)$^b$ | 3.8 | 5.7 | 8.5 | 9.7 | 7.6 | 4.6 | 3.3 | 3.3 |
| $M_{\rm WD}$ (M$_\odot$) | | | | | $0.92^d$ | | | |
| $\log(a)_{07S}$ (g cm$^{-2}$ s$^{-1}$) | | | | | $3.4^d$ | | | |
| $\log(a)_{14S}$ (g cm$^{-2}$ s$^{-1}$) | | | | | $3.3^d$ | | | |
| $\log(a)_{14N}$ (g cm$^{-2}$ s$^{-1}$) | | | | | $0.5^d$ | | | |
| $Z$ ($Z^c_\odot$) | | | | | $0.34^d$ | | | |
| $i$ (°) | $48.1^{+2.6}_{-2.9}$ | $47.6^{+2.6}_{-3.2}$ | $55.2^{+2.3}_{-2.3}$ | $63.0^{+1.6}_{-2.0}$ | $63.1^{+1.6}_{-2.0}$ | $59.1^{+1.9}_{-2.0}$ | $55.7^{+2.2}_{-2.2}$ | $52.1^{+2.2}_{-2.6}$ |
| $\chi^2_{\rm red}$ (d.o.f.) | 1.19 (797) | 1.12 (795) | 1.20 (785) | 1.24 (773) | 1.19 (779) | 1.18 (784) | 1.20 (791) | 1.26 (791) |

*The errors indicate a 90 per cent statistical uncertainty. [a]Ratio of $N_{\rm H,\,07S}$ was fixed at 1.03. [b]Ratio of $N_{\rm H,\,07S}$ was fixed at 0.88.
[c]Based on Anders & Grevesse (1989).
[d]Fixed at the quantity best fitted to the averaged spectrum with PHABS × ($\mathrm{ACRAD_{TH}}$ + $\mathrm{ACRAD_{REF}}$) separating $a$ and normalization using the data set.

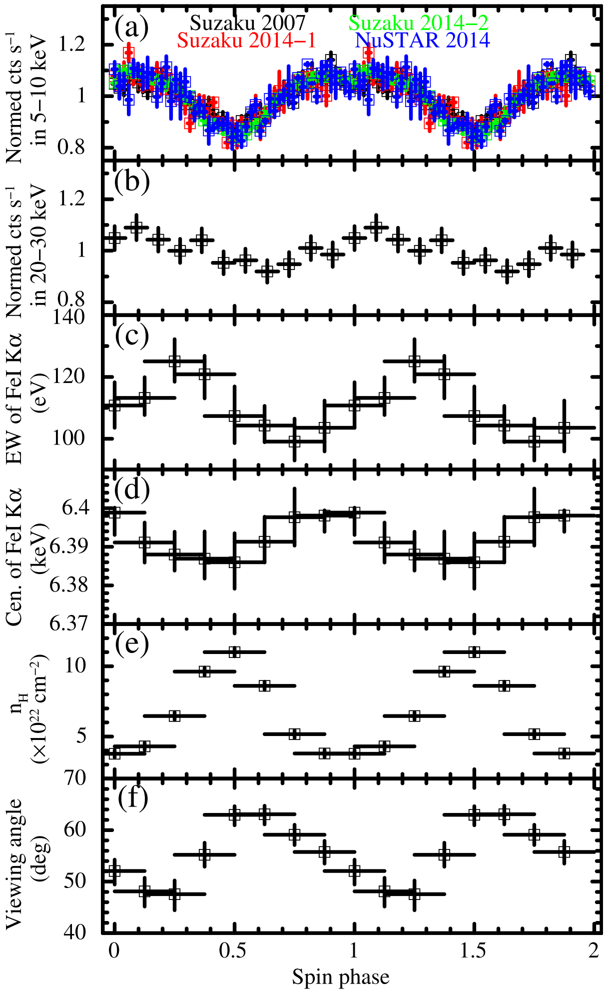


**Figure 5.** Modulations of several parameters in the spin period: (a) 5–10 keV folded light curves of 07S (black), 14S-March (red), 14S-April (green), and 14N (blue), (b) 20–30 keV folded light curve of 14N, (c) EW of the fluorescent iron K $\alpha$ line, (d) centroid of fluorescent iron K $\alpha$ line, (e) hydrogen column density of S07, and (f) the viewing angle. The error bars in (a) and (b) denote a 68 per cent statistical uncertainty, and those of the other panels denote a 90 per cent statistical uncertainty. (c) and (d): Outputs of the PHABS × (POWERLAW + 3 × GAUSSIANS) fitting. (e) and (f): Outputs of `IP-reflect` fitting.

over, `IP-reflect` has fluorescent lines of neutral iron and nickel, unlike the PCA and REFLECT. Therefore, negative line structures are found at the energies of the fluorescent lines (6.404, 6.391, 7.058, 7.478, 7.461, and 8.265 keV for iron K $\alpha_{1,2}$, iron K $\beta$, nickel K $\alpha_{1,2}$, and nickel K $\beta$, respectively).

### 4.2 WD mass estimation

In this section, we correct the estimated WD mass by considering the finite inner disc radius described in Section 4.2.1. In Sections 4.2.2–4.2.4, we discuss several factors that affect the WD mass measurement and summarize the directions in Table 5. We compare the results with an optical measurement technique in Section 4.2.5.

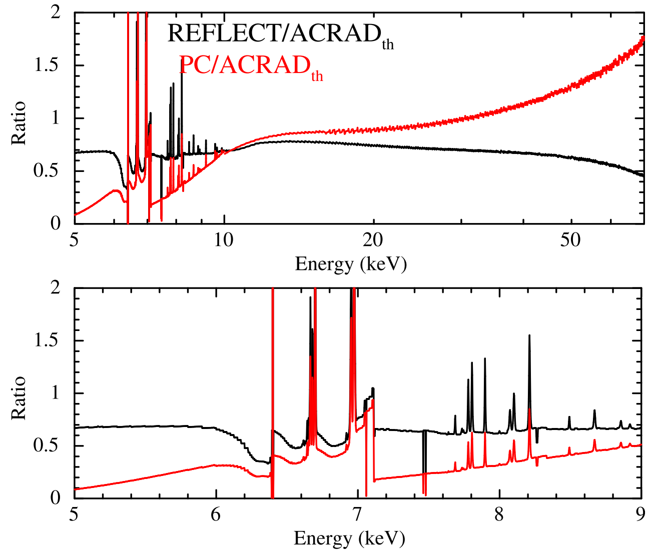


**Figure 6.** Spectral model ratios of the reflection component reproduced by REFLECT (black) and PCFABS (red) to that by ACRAD$_{REF}$. The model spectra above and below 10 keV are the best-fitting models for FPMA and XIS-FI, respectively. The bottom panel shows a blowup of the top between 5 and 9 keV.

#### 4.2.1 *Finite inner disc radius*

`IP-reflect` assumes that accreting gas falls from infinity. Therefore, a non-negligible small inner radius results in a small shock energy release, a low shock temperature, and an underestimation of the WD mass (Suleimanov et al. 2005; Suleimanov, Doroshenko & Werner 2019). The inner disc radius may be approximated by the co-rotation radius,

$$R_{co} = \left( \frac{G M_{WD} P_{spin}^2}{4\pi^2} \right)^{\frac{1}{3}} \quad (2)$$

in the spin equilibrium systems (King & Lasota 1991; King 1993; Shaw et al. 2018). With a spin period of 745.63 s and our WD mass estimate of 0.92 $M_\odot$, the inner radius is estimated as $R_{in} \sim R_{co} = 20\,R_\odot$, where the WD radius is computed by the relation between the WD mass and radius by Nauenberg (1972). As a result, the WD mass should be corrected by 5 per cent to 0.97 $M_\odot$.

#### 4.2.2 *Energy band*

The fitting energy band is a major factor in measuring the WD mass. Because the maximum temperature of an IP is generally higher than 10 keV (e.g. Yuasa et al. 2010), we selected the hard X-ray spectrum (Hailey et al. 2016). Fig. 7 shows the relation between the computed WD mass and the upper limit of the energy band fitted with `IP-reflect` by separating $a$, $N_H$, and the normalization when applying the data set. The computed WD mass converges on 0.92 $M_\odot$ at an upper limit of approximately 50 keV. This is natural because the maximum temperature of the plasma in V1223 Sgr is approximately 40 keV. *NuSTAR* is sufficiently powerful to measure the WD mass in an IP because it gives us high-quality data of up to 78 keV.

The lower limit of the energy band is also important. The emission lines at below 10 keV allow us to measure the metal abundance and the emission measure distribution across the PSAC. The absorption in an IP is created by the complicated accretion curtain and is generally difficult to model. From an observational view, a few partial covering

**Table 5.** Influence of different factors on the estimation of the WD mass.

| Parameter | Direction |
|---|---|
| Upper limit of the energy band | It cannot be too high, and the higher, the better. It should be higher than the maximum plasma temperature at least. It should be adjusted to each target by confirming that the WD mass converges as by Fig. 7. |
| Lower limit of the energy band | It should be high enough to approximate the multicolumnar absorber by a single-column absorber but include the iron K $\alpha$ lines. It has to be adjusted to each target by confirming that the WD mass converges as by Fig. 8. |
| Reflection | It can be reproduced by the AGN reflection model (REFLECT) or by the PCA model instead of the IP reflection model. Note that this substitution is not necessarily valid, with a better energy resolution than that of the CCD. |
| Abundance | It should be parameterized and free in the spectral fitting. |

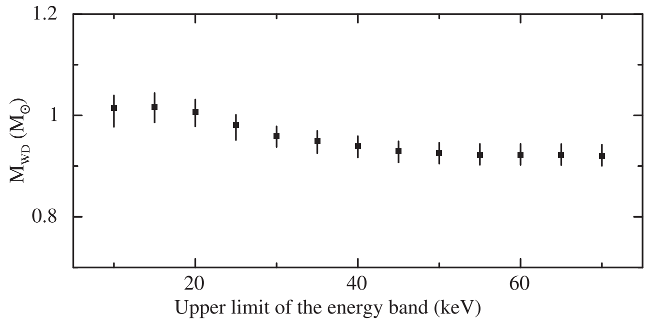


**Figure 7.** WD mass computed by varying the upper limit of the fitted energy band.

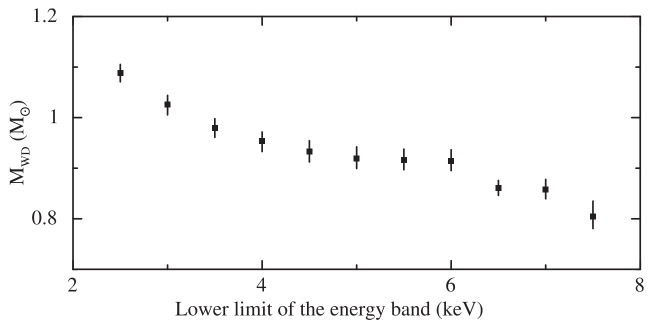


**Figure 8.** WD mass computed by varying the lower limit of the fitted energy band.

absorbers are needed to reproduce the IP spectra at even below 10 keV (Ezuka & Ishida 1999). One method used to avoid this difficulty is cutting off a lower energy band (Ezuka & Ishida 1999). Fig. 8 shows the relation between the computed WD mass and the lower limit of the energy band. Except for the lower limit which is higher than 6 keV, the WD mass converges to 0.92 $M_\odot$. At approximately the 5 keV lower limit, the multicolumnar absorber is approximated using our applied single-column absorber. When the lower limit goes beyond 6 keV (i.e. the iron K $\alpha$ shell band), the emission measure distribution in the temperature cannot be determined and the WD mass estimation suffers from large systematic errors.

### *4.2.3 Abundance*

The abundance is another major factor in measuring the WD mass. In Shaw et al. (2018), the authors measured the WD mass in V1223 Sgr to be 0.75 ± 0.02 or 0.78 ± 0.01 $M_\odot$, which is less massive than our estimate by approximately 0.15 $M_\odot$ with the `IP-reflect` model. The authors excluded the iron K $\alpha$ band (5.5–7.5 keV) and fixed the abundance at 1 $Z_\odot$. Fig. 9 shows the relation between the computed

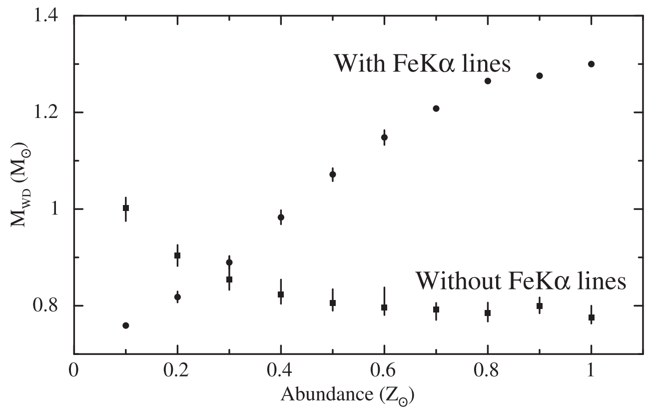


**Figure 9.** Computed WD mass with fixed abundance. Squares show the data fitting without an iron K $\alpha$ band. Circles show the data fitting with the iron K $\alpha$ band. Errors of a part of circles are not shown (see the text).

WD mass and the fixed abundance. By excluding the iron K $\alpha$ band and fixing the abundance at 1 $Z_\odot$, we obtained the WD mass of $M_{\rm WD} = 0.78^{+0.02}_{-0.01}\,M_\odot$, which agrees with Shaw et al. (2018). The lighter WD is computed with higher abundance because the higher abundance leads to a harder reflection continuum (Hayashi et al. 2018). The `AGN-reflect`, which was used by Shaw et al. (2018), model includes this effect as well. However, when we include the iron K $\alpha$ band, such a high abundance of 1 $Z_\odot$ is rejected (reduced-$\chi^2$ = 2.9). Some circles in Fig. 9 do not have an error bar because the $\chi^2$ of the fittings was too large. With the iron K $\alpha$ band, an overabundance leads to an overestimation of the WD mass and an underestimation of the specific accretion rate, and thus the emission line in the thermal and reflection spectra weakens and resembles the data.

### *4.2.4 Reflection component*

To reproduce the reflection spectrum, we used three models, that is, ACRAD$_{\rm REF}$ of `IP-reflect`, REFLECT of `AGN-reflect`, and PCA of `PCA-reflect`. The differences in the best-fitting WD mass are only within 0.04$M_{\rm WD}$ among the models. This result is consistent with that of Cropper et al. (1998) in that the difference in the measured WD masses is 0.04 $M_\odot$ on average at over 13 mCVs with and without the reflection model. However, as mentioned in Section 4.1, the `reflect` and PCA models suppress the reflection in the fitted model, and the degree of the suppression depends on the energy resolution. The data that we used had a modest energy resolution, whereas the *Ginga* data used in Cropper et al. (1998) had an even worse energy resolution. Therefore, we cannot judge whether reflection modelling generally influences the WD mass estimation.

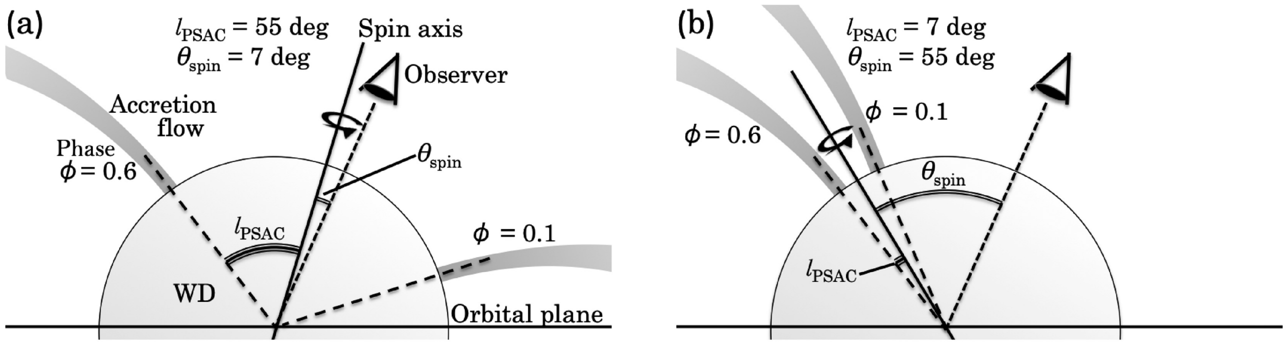


**Figure 10.** Geometries of the WD, PSAC, spin axis, and line of sight in V1223 Sgr. (a) and (b): Cases of ($l_{\rm PSAC}$, $\theta_{\rm spin}$) = (55°, 7°), and (7°, 55°), respectively. The system inclination is 24° (Beuermann et al. 2004) in both cases.

#### 4.2.5 *Comparison with optical estimation*

Penning (1985) estimated the WD mass at 0.4–0.6 $M_\odot$ using an optical orbital modulation measurement. However, in our study, the maximum plasma temperature of V1223 Sgr is estimated as 48 keV and is no less than 30 keV in previous studies using a multitemperature plasma model. As long as the Rankine–Hugoniot relations and the theoretical WD mass–radius relation are valid, the WD of 0.6 $M_\odot$ leads to 22 keV plasma even if the shock is strong and formed at the WD surface. Therefore, the 0.4–0.6 $M_\odot$ should be an underestimation.

### 4.3 Spin modulations of the parameters

We discovered modulations of the EW of the fluorescent iron K $\alpha$ line and viewing angle. The viewing angle approximately anticorrelates with the EW and flux within the 20–30 keV energy band. These anticorrelations are consistent with the fact that lowering the viewing angle enhances the reflection and supports the discovery regarding the viewing angle modulation. If the reflections are a unique factor leading to modulations of the EW and the flux within the 20–30 keV energy band, the modulations would anticorrelate completely with that of the viewing angle. However, the pre-shock gas may also contribute to the modulations, and thus may shift the phase of the modulations. The fluorescent iron K $\alpha$ lines of the EW of ~15 and 40 eV are emitted from the pre-shock gas of $N_{\rm H} = 4 \times 10^{22}$ and $10^{23}$ cm$^{-2}$, respectively (Hayashi et al. 2011), assuming that the pre-shock gas covers the plasma by $2\pi$. The pre-shock gas modulates the 20–30 keV flux by absorption and scattering by a few percentage points. These effects are minor relative to the reflection but should shift the phase.

A sinusoid approximates the viewing angle modulation with average and semi-amplitude values of 55° and 7°, respectively. Its minimum and maximum values are located at spin phases $\phi = 0.1$ and 0.6, respectively. Two combinations of the latitude of the PSAC ($l_{\rm PSAC}$) and the spin axis angle from the line of sight ($\theta_{\rm spin}$) are possible, that is, ($l_{\rm PSAC}$, $\theta_{\rm spin}$) = (55°, 7°), and (7°, 55°), as shown in Fig. 10. Both spin axes disagree with the reported system inclination of 17–47° (Beuermann et al. 2004). This disagreement implies that WD does not receive a substantial fraction of the angular momentum of the accreting gas. At this point, we cannot distinguish between the two geometries, but we may see variations in the angle between the magnetic pole and the PSAC, and distinguish between them if we measure $l_{\rm PSAC}$ and $\theta_{\rm spin}$ more precisely.

The maximum viewing angle phase does not correspond to that of the maximum X-ray. The anticorrelation between the X-ray flux and hydrogen column density agrees with the standard scenario, where the pre-shock gas leads to X-ray modulation by photoelectric absorption (Rosen, Mason & Cordova 1988). This scenario expects that the X-ray flux reaches the maximum when the PSAC points away from the observer and the viewing angle is at its maximum. However, we show that the viewing angle is close to its minimum, rather than its maximum. Some complicated factors, such as unevenness in the density and/or the accretion geometry, should exceed the path-length factor.

We confirmed the central energy modulation of the fluorescent iron K $\alpha$ line reported by Hayashi et al. (2011). The authors suggested that the energy shift is due to the Doppler effect of the pre-shock gas accreting at ~$5 \times 10^3$ km s$^{-1}$. By contrast, `IP-reflect` does not require additional components around the 6.3 keV energy band, as reported, and the Compton shoulder compensates this component. Higher energy resolution data are required to distinguish between these scenarios.

### 4.4 Specific accretion rate and shock height

A fitting of the data with `IP-reflect` by separating the specific accretion rate shows that the parameter changes by the data set as $\log(a_{\rm 07S}\,[{\rm g\,cm^{-2}\,s^{-1}}]) > 1.7$, $\log(a_{\rm 14S}\,[{\rm g\,cm^{-2}\,s^{-1}}]) > 2.3$, and $(a_{\rm 14N}\,[{\rm g\,cm^{-2}\,s^{-1}}]) = 0.5^{+0.3}_{-0.2}$. The luminosity of the three data sets is (1.1–1.2) $\times 10^{34}$ erg s$^{-1}$, indicating that the accretion rate hardly changes. Therefore, the fractional accreting area (*f*, the ratio of the PSAC cross-section to the entire WD area) should be changed to explain the change in the specific accretion rate.

Herein, we examine the consistency in the measured specific accretion rate, hydrogen column density, and area fraction. With a free fall, the velocity of the pre-shock gas can be expressed as

$$v = \sqrt{\frac{2GM_{\rm WD}}{r}}, \quad (3)$$

where $r$ is the distance from the WD centre. The dipole geometry constrains the PSAC cross-section as

$$S = S_0 \left(\frac{r}{R_{\rm WD}}\right)^3, \quad (4)$$

where $S_0$ is the PSAC cross-section at the WD surface. From the mass continuity equation, $\rho v S = a S_0 =$ constant, the density is calculated as

$$\rho = \frac{a R_{\rm WD}^3}{\sqrt{2GM_{\rm WD}}} r^{-\frac{5}{2}}. \quad (5)$$

When the PSAC is sufficiently short, we integrate equation (5) and obtain the mass column density as

$$\sigma = \frac{2aR_{\rm WD}^3}{3\sqrt{2GM_{\rm WD}}}(R_{\rm WD}^{-\frac{2}{3}} - r^{-\frac{2}{3}}). \quad (6)$$

The hydrogen column density can then be obtained as

$$n_{\rm H} = \frac{\sigma}{m_{\rm H}}, \quad (7)$$

where $m_{\rm H}$ is the hydrogen mass. Assuming that the X-rays pass through a path whose length is the radius of the PSAC cross-section, computed from $f$ in Table 3, the specific accretion rates of the data sets 07S, 14S, and 14N ($a$ in Table 3) produce hydrogen column densities of approximately $7.9 \times 10^{22}$, $17 \times 10^{22}$, and $2.0 \times 10^{22}\,{\rm cm}^{-2}$, respectively. These quantities correspond to their respective directly measured hydrogen column density by a factor of 2, and the parameters are approximately self-consistent.

In any case, it is difficult to determine the specific accretion rate (Hayashi & Ishida 2014b). We will obtain new information on the specific accretion rate and the area fraction with a higher energy resolution from the *X-ray Imaging and Spectroscopy Mission* and X-ray polarization from the *Imaging X-ray Polarimeter Explorer*.

## 5 CONCLUSION

We applied the newly developed IP X-ray thermal and reflection spectral models (ACRAD$_{\rm TH}$ + ACRAD$_{\rm REF}$ called `IP-reflect`) to the V1223 Sgr combined spectrum collected from the *Suzaku* satellite in 2007 and 2014, and the *NuSTAR* satellite in 2014. We compared our model with an AGN reflection model (REFLECT with ACRAD$_{\rm TH}$, called `AGN-reflect`) and a PCA model (PCFABS with ACRAD$_{\rm TH}$, called `PCA-reflect`). In this study, `IP-reflect` agrees with other models for the estimated WD mass. This result shows that the reflection modelling does not significantly influence the WD mass measurement in the case of V1223 Sgr, which has a moderate energy resolution ($\Delta E \gtrsim 150$ eV).

In addition, `AGN-reflect` shows a serious self-inconsistent behaviour. The PSAC height determined by the best-fitting solid angle was found to be higher than that calculated hydrodynamically using the best-fitting WD mass and the specific accretion rate by a few orders of magnitude. This problem is probably due to the neglect of the energy loss by the incoherent scattering at below 10 keV. Data with better energy resolution may make the origin of this issue clearer.

We fitted `IP-reflect` by separating the specific accretion rate and hydrogen column density into different data sets. The WD mass, metal abundance, and viewing angle were estimated to be $M_{\rm WD} = 0.92 \pm 0.02\,{\rm M}_\odot$, $Z = 0.34 \pm 0.01\,{\rm Z}_\odot$, and $i = 53.2 \pm 2.1^\circ$, respectively. The three data sets agree on the hydrogen column density as $N_{\rm H,07S} = 6.3^{+0.8}_{-0.9} \times 10^{22}\,{\rm cm}^{-2}$, $N_{\rm H,14S} = (6.5 \pm 0.5) \times 10^{22}\,{\rm cm}^{-2}$, and $N_{\rm H,14N} = 5.5^{+1.2}_{-1.1} \times 10^{22}\,{\rm cm}^{-2}$. By contrast, the specific accretion rate of *NuSTAR* in 2014, $\log(a_{\rm 14N}\,[{\rm g\,cm^{-2}\,s^{-1}}]) = 0.5^{+0.3}_{-0.2}$, is lower than those of the other data ($\log(a_{\rm 07S}\,[{\rm g\,cm^{-2}\,s^{-1}}]) > 1.7$ and $\log(a_{\rm 14S}\,[{\rm g\,cm^{-2}\,s^{-1}}]) > 2.3$). These specific accretion rates constrain the PSAC height as $h_{\rm 07S} < 4 \times 10^{-3}\,R_{\rm WD}$, $h_{\rm 14S} < 9 \times 10^{-4}\,R_{\rm WD}$, and $h_{\rm 14N} = 5^{+4}_{-2} \times 10^{-2}\,R_{\rm WD}$. If the inner disc radius is approximated by the co-rotation radius $R_{\rm in} \sim R_{\rm co} = 20\,{\rm R}_\odot$, the WD mass should be corrected to $0.97 \pm 0.02\,{\rm M}_\odot$. The change in the specific accretion rate results in a change in the fractional accreting area because the thermal X-ray luminosity is $(1.1–1.2) \times 10^{34}\,{\rm erg\,s^{-1}}$ across all data sets. The directly measured hydrogen column densities are approximately consistent with those calculated with the specific accretion rate and fractional accreting area by a factor of 2.

The energy band and the metal abundance affect the WD mass measurement, and the choice of incorrect value introduces large systematic errors (e.g. $\lesssim 0.2\,{\rm M}_\odot$ in the WD mass). Without an energy of higher than 40 keV, it was difficult to measure the maximum temperature, which is essential for the WD mass measurement. The spectrum at below 5 keV introduces a complication of the multicolumnar absorber. The iron K $\alpha$ energy band is also essential to determine the emission measure as a function of temperature. Incorrect metal abundance leads to overintensity or underintensity of the hard X-ray continuum and emission lines, resulting in a large error in the WD mass measurement.

We fitted an empirical model composed of a power law and three Gaussians or `IP-reflect` to the spin-phase-resolved spectra. With `IP-reflect`, the WD mass, metal abundance, specific accretion rate, and ratio of the hydrogen column density between the data sets were fixed to those of the best-fitting parameters of the average spectral fitting. We discovered for the first time the modulation of the EW and viewing angle. The viewing angle anticorrelates approximately with the EW and flux within the 10–30 keV energy band. This fact supports the discovery of the viewing angle modulation by `IP-reflect`.

The viewing angle modulation has average and semi-amplitude values of 55° and 7°, respectively. Two combinations of the latitude of the PSAC ($l_{\rm PSAC}$) and the spin axis angle from the line of sight ($\theta_{\rm spin}$) are possible, that is, ($l_{\rm PSAC}$, $\theta_{\rm spin}$) = (55°, 7°) or (7°, 55°). In either case, the spin axis disagrees with the previously reported system inclination of 24° (Beuermann et al. 2004).

The anticorrelation between the viewing angle and the flux is inconsistent with the expectation of the standard model, which is called the accretion curtain model. For V1223 Sgr, a complex structure in the pre-shock gas, e.g. the unevenness of the density, should affect the X-ray modulation.

## ACKNOWLEDGEMENTS

The authors are grateful to all of the *Suzaku* and *NuSTAR* project members for developing the instruments and their software, the spacecraft operations, and the calibrations. We thank the anonymous referee and Dr. Yang Soong for their careful review and insightful comments, and Editage (www.editage.com) for English language editing. Support for this work was provided by the National Aeronautics and Space Administration through Chandra Award Number GO9-20022A issued by the Chandra X-ray Center, which is operated by the Smithsonian Astrophysical Observatory for and on behalf of the National Aeronautics Space Administration under contract NAS8-03060.

## DATA AVAILABILITY

The *Suzaku* and *NuSTAR* data used in this study are publicly available in the HEASARC archive at https://heasarc.gsfc.nasa.gov/.

## REFERENCES

Aizu K., 1973, Prog. Theor. Phys., 49, 1184
Anders E., Grevesse N., 1989, Geochim. Cosmochim. Acta, 53, 197
Arnaud K. A., 1996, in George H. J., Jeannette B., eds, ASP Conf. Ser. Vol. 101, Astronomical Data Analysis Software and Systems V. Astron. Soc. Pac., San Francisco, p. 17
Beardmore A. P., Done C., Osborne J. P., Ishida M., 1995, MNRAS, 272, 749

Beardmore A. P., Osborne J. P., Hellier C., 2000, MNRAS, 315, 307
Beuermann K., Harrison T. E., McArthur B. E., Benedict G. F., Gänsicke B. T., 2004, A&A, 419, 291
Boldt E., 1987, Phys. Rep., 146, 215
Brunschweiger J., Greiner J., Ajello M., Osborne J., 2009, A&A, 496, 121
Buckley D. A. H., Sekiguchi K., Motch C., O'Donoghue D., Chen A.-L., Schwarzenberg-Czerny A., Pietsch W., Harrop-Allin M. K., 1995, MNRAS, 275, 1028
Canalle J. B. G., Saxton C. J., Wu K., Cropper M., Ramsay G., 2005, A&A, 440, 185
Cropper M., Ramsay G., Wu K., 1998, MNRAS, 293, 222
Cropper M., Wu K., Ramsay G., Kocabiyik A., 1999, MNRAS, 306, 684
Das U., Mukhopadhyay B., Rao A. R., 2013, ApJ, 767, L14
Ezuka H., Ishida M., 1999, ApJS, 120, 277
Fujimoto R., Ishida M., 1997, ApJ, 474, 774
Fukazawa Y. et al., 2009, PASJ, 61, 17
Gaia Collaboration, 2016, A&A, 595, A1
George I. M., Fabian A. C., 1991, MNRAS, 249, 352
Hailey C. J. et al., 2016, ApJ, 826, 160
Harrison F. A. et al., 2013, ApJ, 770, 103
Hayashi T., Ishida M., Terada Y., Bamba A., Shionome T., 2011, PASJ, 63, 739
Hayashi T., Ishida M., 2014a, MNRAS, 438, 2267
Hayashi T., Ishida M., 2014b, MNRAS, 441, 3718
Hayashi T., Kitaguchi T., Ishida M., 2018, MNRAS, 474, 1810
Hōshi R., 1973, Prog. Theor. Phys., 49, 776
Imamura J. N., Durisen R. H., 1983, ApJ, 268, 291
Ishida M., Silber A., Bradt H. V., Remillard R. A., Makishima K., Ohashi T., 1991, ApJ, 367, 270
King A. R., 1993, MNRAS, 261, 144
King A. R., Lasota J.-P., 1991, ApJ, 378, 674
Kokubun M. et al., 2007, PASJ, 59, 53
Koyama K. et al., 2007, PASJ, 59, 23
Landi R. et al., 2009, MNRAS, 392, 630
Magdziarz P., Zdziarski A. A., 1995, MNRAS, 273, 837
Mitsuda K. et al., 2007, PASJ, 59, S1
Mukai K., Rana V., Bernardini F., de Martino D., 2015, ApJ, 807, L30
Nauenberg M., 1972, ApJ, 175, 417
Osborne J. P., Rosen R., Mason K. O., Beuermann K., 1985, Space Sci. Rev., 40, 143
Penning W. R., 1985, ApJ, 289, 300
Ramsay G., Potter S., Cropper M., Buckley D. A. H., Harrop-Allin M. K., 2000, MNRAS, 316, 225
Rosen S. R., Mason K. O., Cordova F. A., 1988, MNRAS, 231, 549
Saxton C. J., Wu K., Cropper M., Ramsay G., 2005, MNRAS, 360, 1091
Saxton C. J., Wu K., Canalle J. B. G., Cropper M., Ramsay G., 2007, MNRAS, 379, 779
Serlemitsos P. J. et al., 2007, PASJ, 59, 9
Shaw A. W., Heinke C. O., Mukai K., Sivakoff G. R., Tomsick J. A., Rana V., 2018, MNRAS, 476, 554
Suleimanov V., Revnivtsev M., Ritter H., 2005, A&A, 435, 191
Suleimanov V. F., Doroshenko V., Werner K., 2019, MNRAS, 482, 3622
Takahashi T. et al., 2007, PASJ, 59, 35
Terada Y., Enoto T., Miyawaki R., Ishisaki Y., Dotani T., Ebisawa K., Ozaki M., 2008, PASJ, 60, S25
van Teeseling A., Kaastra J. S., Heise J., 1996, A&A, 312, 186
Woelk U., Beuermann K., 1996, A&A, 306, 232
Wu K., Chanmugam G., Shaviv G., 1994, ApJ, 426, 664
Yoon S.-C., Langer N., 2004, A&A, 419, 623
Yuasa T., Nakazawa K., Makishima K., Saitou K., Ishida M., Ebisawa K., Mori H., Yamada S., 2010, A&A, 520, A25

This paper has been typeset from a TEX/LATEX file prepared by the author.